Bridging closed and dissipative discrete time crystals in spin systems with infinite-range interactions

Jayson G. Cosme*

National Institute of Physics, University of the Philippines, Diliman, Quezon City 1101, Philippines

Jim Skulte and Ludwig Mathey

Zentrum für Optische Quantentechnologien and Institut für Laser-Physik, Universität Hamburg, 22761 Hamburg, Germany and The Hamburg Center for Ultrafast Imaging, Luruper Chaussee 149, 22761 Hamburg, Germany (Dated: March 24, 2023)

We elucidate the role of dissipation on the emergence of time crystals in a periodically driven spin system with infinite-range interactions. By mapping out the phase diagrams for varying dissipation strengths, ranging from zero to infinitely strong, we demonstrate that the area in the phase diagram, where a time crystal exists, grows with the dissipation strength, but only up to an optimal point, beyond which most of the time crystals become unstable. We find signatures of time crystalline phases in both closed-system and dissipative regimes under the right conditions. However, the dissipative time crystals are shown to be more robust against random noise in the drive, and are only weakly affected by the choice of initial state. We present the finite-size behaviour and the scaling of the lifetime of the time crystals with respect to the number of spins and the interactions strength, within a fully quantum mechanical description.

I. INTRODUCTION

A time crystal (TC) is a nonequilibrium phase of matter signified by the spontaneous breaking of time-translation symmetry [1–5]. This characteristic behaviour manifests itself in the emergence of a periodic pattern in time distinct from the underlying temporal symmetry of the system. For example, a TC in a system described by a periodically driven Hamiltonian $H(t) = H(t+T_d)$, where T_d is the driving period, will display an observable \hat{O} oscillating at a lower frequency or higher period, i.e., $\langle \hat{O}(t) \rangle = \langle \hat{O}(t + nT_d) \rangle$ with n > 1. Time crystals (TCs) are formed through an interplay between periodic driving, many-body interactions, and, possibly, dissipation. Initial predictions and subsequent realisations of TCs involve closed systems, wherein tailored interactions and strong disorder prevent heating dynamics that would otherwise destabilise a TC [6–22]. Controlled dissipation has also been demonstrated as an alternative strategy for stabilising TCs [23–38]. In most of these physical systems, time crystalline dynamics can be understood using the spin language [6–19, 23–33].

Focusing on fully connected spin systems, or equivalently, spins with all-to-all interactions, time crystalline phases have been studied both for closed and dissipative systems through the Lipkin-Meshkov-Glick (LMG) model and the open Dicke model, respectively. Originally introduced in the context of nuclear physics [39–41], the LMG model describes N fully connected spin-1/2 particles in a transverse field. A similar model for photon-mediated interactions is the Dicke model (DM) [42]. The DM typifies a spin-boson system, wherein the bosons, specifically, photons in a single mode, mediate the all-to-all interactions between the spins [43, 44]. The open version of the DM includes a dissipation channel via the photon decay. On the one hand, discrete TCs and the related subharmonic response are predicted to exist in the periodically driven closed LMG model [9, 10, 45]. We note that a direct

experimental observation of a TC in such an infinite-range interacting closed system remains elusive, even though existing platforms could in principle simulate the LMG model, for example, in Refs. [46–49]. On the other hand, the paradigmatic discrete TC in open systems is proposed in the driven-dissipative Dicke model [23, 24]. Using a cavity-QED platform as a quantum simulator of the open DM, indeed, a Dicke time crystal has been realised experimentally [37], despite the mean-field breaking terms in cavity-QED systems that compete with the infinite-range interactions necessary for emulating the DM [50].

In the limit of an extremely strong photon decay rate $\kappa \to \infty$, adiabatic elimination of the rapidly evolving photon field will map the open DM onto the closed LMG model, which establishes the relation between these two fully connected models [44, 51, 52]. However, it has been suggested for selected parameters that too strong dissipation could be detrimental to the stability of TCs in the open DM [23, 24], which then poses the question how this relates to the time crystal phenomenology in the closed LMG model [9, 10]. As we will show later, the precise form of driving and the choice of the initial state become crucial in the closed-system limits of vanishing and infinitely strong dissipation rates. In contrast, we will demonstrate that the time crystalline dynamics occur more ubiquitously in the dissipative regime.

In this work, we present a thorough investigation of TCs in the transition from closed-system to dissipative limits, or vice-versa, for spin systems with infinite-range interactions mediated by photons. By doing so, we shed light on the precise roles of dissipation and the form of driving on the emergence of TCs in infinite-range interacting systems, such as the cavity-QED setup used in the realisation of the dissipative Dicke TC [33]. To describe the system, we use the open DM for weak and intermediate dissipations, and an effective atom-only description and the LMG model for strong dissipations, in which the photons are adiabatically eliminated. We consider a binary drive, wherein the system periodically switches between interacting and noninteracting Hamiltonians as shown in Fig. 1(a). Mapping out the phase diagrams for

^{*} jcosme@nip.upd.edu.ph

a range of dissipation strengths $\kappa \in [0, \infty)$, we connect the TCs in the closed and dissipative regimes, and demonstrate that the areas in the phase diagram with time crystals and time quasicrystals (TQCs) expand with increasing dissipation but only up to an optimal value as depicted in Figs. 1(c)-1(d). We also find numerical evidence suggesting that the mechanism for generating TCs in the dissipative system is a period-doubling instability arising from a parametric resonance, and therefore we generalise the conditions first proposed in Ref. [23]. Furthermore, the TCs in the open DM are found to be more robust against random errors in the drive and are less sensitive to the choice of initial states compared to their counterparts in the closed-system limits, $\kappa=0$ and $\kappa \to \infty$. Nevertheless, the TCs in the closed LMG model display enhanced stability for few spins, wherein quantum effects dominate, as their lifetimes can be increased by simply increasing the interactions strength without changing the number of spins, and they have longer lifetimes than the TCs in the open DM, in general.

This work is organised as follows. In Sec. II, we introduce the relevant physical models, namely the Dicke model, its atom-only description, and the LMG model, and the driving protocol. In Sec. III, we explore using mean-field theory the dynamical phase diagrams for varying dissipation strengths, and the robustness of time crystals against noises in the drive and choices of initial states. In Sec. IV, we investigate the properties of time crystals for both closed-system and dissipative limits in the quantum regime of few spins. Finally, we conclude in Sec. V.

II. MODELS AND DRIVING PROTOCOL

The Hamiltonian for the open Dicke model is [43]

$$\hat{H}/\hbar = \omega_p \hat{a}^{\dagger} \hat{a} + \omega_0 \hat{J}_z + \frac{2\lambda}{\sqrt{N}} \left(\hat{a}^{\dagger} + \hat{a} \right) \hat{J}_x, \tag{1}$$

where N is the total number of spins, \hat{a} (\hat{a}^{\dagger}) is the bosonic annihilation (creation) operator for the photons, and $\hat{J}_{\mu} = \sum_{i=1}^{N} \sigma_{i}^{\mu}$ ($\mu = x, y, z$) are the collective spin operators. The light-matter coupling strength is λ , the photon frequency is ω_{p} , and the transition frequency of the two-level atoms represented by the spins operators is ω_{0} . In the presence of photon losses, the dynamics of the system can be described by the Lindblad master equation [53]

$$\partial_t \hat{\rho} = -i[\hat{H}/\hbar, \hat{\rho}] + \kappa D[\hat{a}]\hat{\rho}, \tag{2}$$

where $D[\hat{a}]\hat{\rho}=2\hat{a}\hat{\rho}\hat{a}^{\dagger}-\left(\hat{a}^{\dagger}\hat{a}\hat{\rho}+\hat{\rho}\hat{a}^{\dagger}\hat{a}\right)$. The rate of photon emission is characterised by the photon decay rate or dissipation strength κ .

An effective atom-only description can be obtained for large but finite dissipation strength, $\infty > \kappa \gg \omega_0$ [54, 55], which, in this work, will be called the atom-only Dicke model

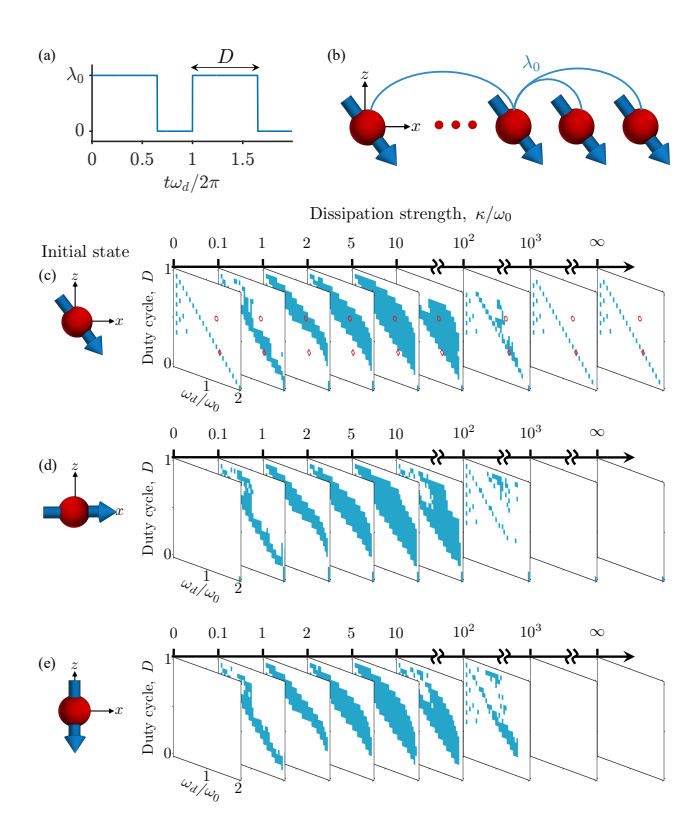


FIG. 1. (a) Driving protocol. The duty cycle, D, is the duration of the "bright time" in one Floquet cycle. (b) During the bright times, photons mediate the all-to-all interactions between the spins. (c)-(d) Dynamical phase diagrams as a function of D and driving frequency ω_d for varying dissipation strengths, κ . The light-matter coupling is fixed at $\lambda_0=1.1\lambda_{\rm cr}$ and the photon frequency is $\omega_p=\omega_0$. As depicted in the left-most panels of (c)-(d), three types of initial product states are considered: (c) one of the \mathbb{Z}_2 -symmetry broken states, (d) spins polarised along the positive x-direction, and (e) spins polarised along the negative z-direction. The dark areas in each phase diagram denote the period-doubling time crystalline phases. We use the Dicke model for $\kappa/\omega_0 \leq 10^3$, the atom-only Dicke model for $10^3 \leq \kappa/\omega_0 < \infty$, and the LMG model for $\kappa = \infty$.

(ADM). The ADM Hamiltonian is [55]

$$\hat{H}_{\text{ADM}}/\hbar = \omega_0 \hat{J}_z - \left(\frac{4\lambda^2 \omega_p}{N(\kappa^2 + \omega_p^2)}\right) \hat{J}_x^2$$

$$- \left(\frac{4\lambda^2 \kappa \omega_p \omega_0}{N(\kappa^2 + \omega_p^2)^2}\right) \{\hat{J}_x, \hat{J}_y\} - \left(\frac{2\lambda^2 \omega_0 (\omega_p^2 - \kappa^2)}{N(\kappa^2 + \omega_p^2)}\right) \hat{J}_z$$
(3)

In the thermodynamic limit, the ADM Hamiltonian yields the correct set of equations of motion first obtained in Ref. [54].

In the limit of $\kappa \to \infty$, the photonic mode can be adiabatically eliminated to obtain a Hamiltonian that depends only on the spins, equivalent to the anisotropic Lipkin-Meshkov-Glick (LMG) model [39–41, 56]

$$\hat{H}_{\rm LMG}/\hbar = \omega_0 \hat{J}_z - \left(\frac{4\lambda^2 \omega_p}{N(\kappa^2 + \omega_p^2)}\right) \hat{J}_x^2. \tag{4}$$

The last term in Eq. (4) reveals that indeed the photons mediate the effective all-to-all interactions between the spins. In

addition to the light-matter coupling strength λ , the parameters related to the photonic degree of freedom, namely the photon frequency ω_p and dissipation rate κ , also contribute to the strength of the effective spin-spin interactions.

In the thermodynamic limit, we rescale $a = \langle \hat{a} \rangle / \sqrt{N}$ and $j_{\mu \in \{x,y,z\}} = \langle \hat{J}_{\mu} \rangle / N$. The three models described above all possess a symmetry breaking phase transition at a critical value of the coupling strength given by [43, 51, 53, 54]

$$\lambda_{\rm cr} = \frac{1}{2} \sqrt{\frac{\omega_0}{\omega_p} (\omega_p^2 + \kappa^2)}.$$
 (5)

Below the critical coupling strength, the stable phase or steady state corresponds to all the spins pointing in the negative z-direction, $\{j_x,j_y,j_z\}=\{0,0,-1/2\}$. This phase is sometimes referred to as the normal phase (NP) and for the Dicke model. Another defining feature of the NP is the absence of photons, a=0. Above the critical coupling strength, the system undergoes a quantum phase transition as it spontaneously breaks the \mathbb{Z}_2 symmetry, $\{\hat{a},\hat{J}_x\} \to \{-\hat{a},-\hat{J}_x\}$. The steady state in the symmetry broken phase has a spin configuration of [53]

$$\{j_x, j_y, j_z\} = \frac{1}{2} \left\{ \pm \sqrt{1 - \left(\frac{\lambda_{\rm cr}^2}{\lambda^2}\right)^2}, 0, -\frac{\lambda_{\rm cr}^2}{\lambda^2} \right\}.$$
 (6)

In the Dicke model, the photon mode is occupied in the symmetry broken phase, also known as the superradiant phase. The corresponding steady-state photon amplitude is

$$a = \mp \frac{\lambda}{\omega - i\kappa} \sqrt{1 - \left(\frac{\lambda_{\rm cr}^2}{\lambda^2}\right)^2}.$$
 (7)

We are interested in a binary Floquet drive or "bang-bang" protocol, wherein the interactions periodically switch according to

$$\lambda(t) = \begin{cases} \lambda_0, & nT_d \le t < (n+D)T_d \\ 0, & (n+D)T_d \le t < (n+1)T_d, \end{cases}$$
 (8)

where $n \in [0, 1, 2, ...]$, T_d is the driving period related to the driving frequency via $\omega_d = 2\pi/T_d$, and $D \in [0,1]$ is a unitless quantity called the duty cycle. The duty cycle controls the duration of the 'dark' ($\lambda = 0$) and 'bright' ($\lambda = \lambda_0$) times in a driving cycle. For D = 0, the the light-matter coupling is always off, while for D=1 the light-matter coupling has a constant nonzero value, λ_0 , for all times. This binary driving protocol has been shown to host a period-doubling dissipative TC for D=0.5 [23, 24]. We note that for $D\to 1$, this protocol is not identical to the kicking protocol considered in Ref. [9], because in Ref. [9], the spins are flipped using a π pulse along the x-direction during the kicking times, i.e., the 'transverse field' ω_0 is driven. Instead of applying a spin-flip operation, we allow the spins to rotate freely according to the coherent time evolution during the dark times, at least for the closed-system or nondissipative regimes.

III. MEAN-FIELD RESULTS

We first consider the thermodynamic or mean-field limit of large number of spins N. In the limit of large number of spins, cavity-QED systems based on quantum gases [57, 58] are ideal platforms for quantum simulations since the typical number of atoms, emulating the two-level systems, reaches $N \sim 10^5$. In fact, various phenomena predicted in the Dicke model ranging from the normal-superradiant phase transition [46, 59] to the formation of dissipative discrete TCs [33] have been observed using quantum-gas-cavity systems.

The mean-field dynamics can be obtained by solving the corresponding semiclassical equations of motion. Depending on the value of κ , we use the appropriate model, i.e., the Dicke model for $\kappa/\omega_0 < 10^3$, the atom-only Dicke model for $10^3 \leq \kappa/\omega_0 < \infty$, and the LMG model for $\kappa = \infty$. The semiclassical equations of motion for the three models are presented in Appendix A. In the following, we numerically integrate the equations of motion and mainly focus on the dynamical behaviour of the expectation value of the total magnetisation along the x-component, j_x . We consider a total driving time of $t_f = 100T_d$ in accordance with the typical timescales in state-of-the-art experiments on closed and dissipative discrete TCs [15–17, 19, 37].

In subsections III A and III B, we choose as the initial state one of the \mathbb{Z}_2 -symmetry broken states amounting to all spins having a non-zero component in the positive x-direction, which is denoted by the upper sign solution in Eq. (6). For the Dicke model, the additional initial condition for the photon amplitude is given by Eq. (7). In subsection III C, we investigate other types of initial states, namely spins that are fully polarised either along the positive x-direction or the negative z-direction. We fix the light-matter coupling to $\lambda_0 = 1.1\lambda_{\rm cr}$ and the photon frequency to $\omega_p = \omega_0$. Fixing $\lambda_0/\lambda_{\rm cr}$ makes the results for the LMG model independent of ω_p and κ since the interaction strength in the LMG Hamiltonian Eq. (4) only depends on this ratio. In Appendix C, we show similar results for other choices of λ and ω_p .

A. Dynamical phases

A generic many-body system with periodic driving, especially in the absence of dissipation, is expected to inevitably heat up and approach a featureless state [60, 61]. Time crystals in closed systems are particularly interesting since they are exception to this. To distinguish between non-trivial phases and a thermal or chaotic phase, we define the decorrelator

$$d = \frac{1}{(t_f - t_i)} \sum_{t=t_i}^{t_f} \left(|j_x(t)| - |j_x'(t)| \right), \tag{9}$$

where $j_x'(t)$ is the dynamics of a slightly perturbed initial state relative to $j_x(t)$. Specifically, we choose $j_x'(0) = j_x(0) - 0.5 \times 10^{-3}$, $j_y'(0) = 0$, and $j_z'(0) = -\sqrt{1-|j_x'(0)|^2}/2$. The decorrelator provides a measure for the distance between the time-evolving observables to probe the emergence of chaos

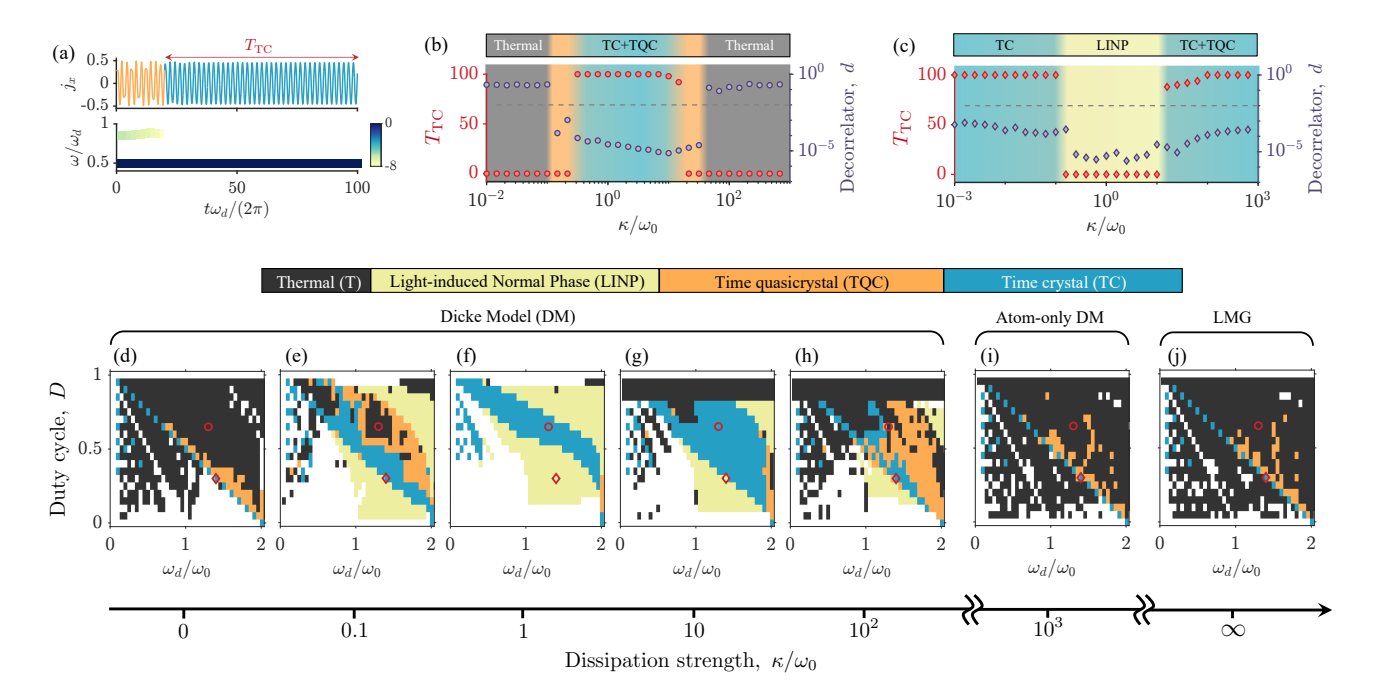


FIG. 2. (a) (Top panel) Exemplary dynamics of j_x for $\kappa/\omega_0=20$ with driving parameters $\{D,\omega_d\}=\{0.3,1.4\omega_0\}$. These driving parameters are denoted as a circle in (d)-(j). The dark curve with duration $T_{\rm TC}$ denotes the period-doubling response while the light curve corresponds to the transient quasi-period-doubling behaviour. (Bottom panel) Corresponding time-frequency power spectrum of j_x in log-scale for the two highest peaks. (b,c) Dependence of the $T_{\rm TC}$ and the decorrelator, d, on the dissipation strength κ for driving parameters marked by (b) circles and (c) diamond in (d)-(j). The driving parameters are (b) $\{D,\omega_d\}=\{0.65,1.3\omega_0\}$ and (c) $\{D,\omega_d\}=\{0.3,1.4\omega_0\}$. The horizontal dashed lines denote d=0.01, which is the threshold used to distinguish between thermal and non-thermal phases. (d)-(j) Various phases identified for different driving parameters D and ω_d . Each panel corresponds to a specific value of κ . Harmonic, superharmonic, and n-tupling dynamics are all represented in the white areas. For the results shown here, the photon frequency and light-matter coupling strength are fixed to $\omega_p=\omega_0$ and $\omega_0=1.1\lambda_{\rm cr}$, respectively.

[62, 63]. A large decorrelator $d \sim 1$ signifies sensitivity to initial conditions consistent with classical chaos. We obtain the decorrelator for a time window spanned by $t_i = 50T_d$ and $t_f = 100T_d$. To classify thermal phases, we set a threshold of $d \geq 0.01$.

In the top panel of Fig. 2(a), we show an exemplary dynamics exhibiting both a time quasicrystal (TQC) for transient times and a period-doubling TC for long times. To quantify the lifetime of the time crystal $T_{\rm TC}$, we calculate a time-frequency power spectrum according to $P(\omega,t)=$ $|\mathcal{F}(\omega,t)|^2/\sum_{i=1}^{N_f}|\mathcal{F}(\omega,t)|^2$, where $\mathcal{F}(\omega,t)$ is the Fourier transform of j_x for the time window starting at time t and ending at $t_f = 100T_d$. The total number of discrete frequencies resolved by the Fourier transform is N_f . To demonstrate how we obtain T_{TC} using $P(\omega, t)$, we present in the bottom panel of Fig. 2(a) an example of the time-frequency power spectrum. A TQC is marked by the appearance of a secondary peak in the power spectrum in addition to the primary peak associated with the period doubling response [62]. We then use the appearance of a secondary peak in the power spectrum with $\log P(\omega, t') > -8$ as a criterion for detecting TQC phases. That is, the lifetime of the TC phase for simulation times considered here is $T_{\rm TC} = 100T_d - t'$. In Fig. 2(a), we indeed find a secondary peak around $t' \approx 20T_d$ consistent with a visual inspection of the dynamics shown in the top panel. Thus, for this example, the system is in a time quasicrystalline phase for t < t' and the TC emerging for t > t' has a lifetime of at least $T_{\rm TC} = 80T_d$.

The lifetime $T_{\rm TC}$ and the decorrelator d as a function of the dissipation strength κ are shown in Figs. 2(b) and 2(c), which correspond to driving parameters $\{D,\omega_d\}=\{0.65,1.3\omega_0\}$ and $\{D,\omega_d\}=\{0.3,1.4\omega_0\}$, respectively. In Fig. 2(b), the values of the decorrelator d for thermal phases are several orders of magnitude larger than those for non-thermal phases. We set $T_{\rm TC}=0$ for thermal phases, regardless of whether a transient TQC is found for early times or a time crystalline signal is detected for a single mean-field trajectory.

For time-translation symmetry breaking responses, we find the following phases: (i) pure TC, (ii) pure TQC, and (iii) mixed TC and TQC. A pure TC is characterised by having period-doubling dynamics for the entire duration of the simulation, $T_{\rm TC}=100T_d$, as exemplified by $\kappa/\omega_0=1$ in Fig. 2(b) and $\kappa/\omega_0=10^{-3}$ in Fig. 2(c). On the other hand, a pure TQC, while insensitive to initial conditions, d<0.01, still has $T_{\rm TC}=0$, since its spectrum has at least one additional subharmonic frequency peak, which in general is incommensurate with the driving frequency, for the entire simulation time. An example of the dynamics and the power spectrum for a pure TQC is $\kappa/\omega_0=21$ shown in Appendix B (see Fig. 9(a)). Lastly, a mixed TC and TQC phase is denoted by a transient TQC at early times and a TC at long times, as shown

in Fig. 2(a) for example. We label the pure TC phase and mixed TC and TQC phase as simply TC for the rest of the paper since both have long-time period-doubling behaviour.

The results presented in Figs. 2(b) and 2(c) highlight one of the key findings of this work, which is the nonmonotonic behaviour in the presence and lifetime of time crystals as a function of the dissipation strength. The optimal dissipation strength will strongly depend on the specific choice of driving parameters. This is illustrated by the absence of time crystals for $\kappa/\omega_0 < 10^{-1}$ and $\kappa/\omega_0 > 10^2$ in Fig. 2(b) while they are present in Fig. 2(c) for the same regimes of dissipation strength . In fact, for intermediate dissipation strengths $10^{-1} < \kappa/\omega_0 < 10^2$, wherein time crystals are seen in Fig. 2(b), the driving parameters in Fig. 2(c) push the system into a light-induced normal phase, which is a normal phase dynamically stabilised by the drive and is defined by having zero photon number despite $\lambda_0 > \lambda_{\rm cr}$ [29] (see also Fig. 9(b) in Appendix B).

In Figs. 2(d)-2(j), the dynamical phase diagrams as a function of the driving parameters are shown, wherein each panel corresponds to a particular choice of dissipation strength κ . That is, we demonstrate in Figs. 2(d)-2(j) how the dynamical phase diagram changes with the dissipation strength. In the following, we will not discuss harmonic, superharmonic, and n-tupling dynamics, which are all indicated by the white areas in the dynamical phase diagrams. Instead, we concentrate on the influence of dissipation on the thermal, time crystalline, and time quasicrystalline phases.

1. Closed systems

We find TC and TQC phases in the closed-system limits, namely the closed DM ($\kappa=0$), the ADM ($\kappa/\omega_0=10^3$), and the LMG model ($\kappa\to\infty$), albeit only in a relatively narrow region of the driving parameter space. The dynamical phase diagrams for closed systems in Figs. 2(d), 2(i), and 2(j) share a strong similarity with each other, especially in the location of the TC phases. The qualitative agreement between the ADM and LMG phase diagrams imply the applicability of the LMG model for dynamical states, such as a TC, which is in contrast to the limitation of the LMG model in describing steady states [54, 55].

The apparent period-doubling response seen for D=0, as illustrated in Fig. 3(a), can be considered trivial since this simply corresponds to a sudden quench at t=0 from $\lambda=1.1\lambda_{\rm cr}$ to $\lambda=0$. Within the LMG model, this leads to a coherent dynamics of the spins precessing around the z-axis at a frequency ω_0 , i.e., a precession period of $T_0=2\pi/\omega_0$. For a driving frequency of $\omega_d=2\omega_0$, such a response will seemingly appear as subharmonic even though the periodic drive is actually absent for D=0 as illustrated in Fig. 3(a).

Based on the location of the TC phases in the phase diagrams in Figs. 2(d), 2(i), and 2(j) that for the closed DM, ADM, and LMG model, we identify that a period doubling instability emerges for bang-bang protocols when the duty cycle

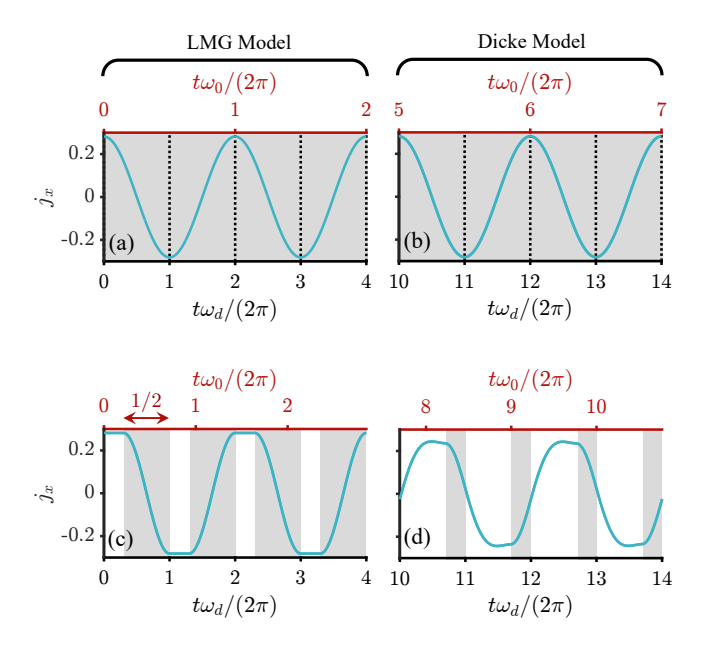


FIG. 3. Dynamics of j_x in the (left panels) LMG model and (right panels) Dicke model with $\kappa/\omega_0=1$. (a),(b) In the absence of driving and for a sudden quench D=0, the spins precess around the z-direction due to the first term in the Hamiltonian in Eq. (4). The top axis displays time in units of the precession period $T_0=\omega_0/(2\pi)$ while the bottom axis shows time in units of the driving period $T_d=\omega_d/(2\pi)$. This apparent period doubling is trivial as the periodic driving is absent. (c),(d) Time crystals for the periodically driven systems with parameters (c) $\{D,\omega_d\}=\{0.3,1.4\omega_0\}$ and (d) $\{D,\omega_d\}=\{0.7,1.3\omega_0\}$. The shaded areas indicate the dark time when the spin interactions are switched off. The arrow in (c) indicates that the dark time is $t_{\rm dark}=T_0/2$. The remaining parameters are the same as in Fig. 2.

follows

$$D_{\rm ins} = 1 - \frac{\omega_d}{2\omega_0}. (10)$$

The above condition appears as a line in the phase diagram and it can be analytically understood as follows. The magnetisation j_x for the noninteracting limit will have the same magnitude but opposite sign as its initial value every $(n+1/2)T_0$, where n is an integer. Hence, for the driven system, the dark time must be exactly half the precession period in the absence of spin interactions, $t_{\rm dark} = T_0/2$. The instability condition Eq. (10) precisely satisfies this:

$$t_{\text{dark}} = (1 - D_{\text{ins}})T_d = \frac{2\pi}{2\omega_0} = \frac{T_0}{2}.$$
 (11)

The state at times $t = (n + 1/2)T_0$ is the symmetry broken partner of the initial state, which is chosen to be an eigenstate of the Hamiltonian with spin-spin interactions. As such, the states do not change during the bright times of each driving cycle as depicted in the white areas in Fig. 3(c), which then yields the apparent period-doubling response for the bangbang protocol. Therefore, the emergence of a period doubling response in the absence of dissipation strongly hinges on the appropriate timing of when the interactions are switched on

and off. This interplay between the internal dynamics of the spins and the timing of the external drive is also argued to be important for the *n*-tupling response in a variable-range interacting spin model with binary driving [45].

In general, for an integer m, the period doubling arises if $t_{\rm dark} = (m+1/2)T_0$. The driving parameters for the isolated islands of TC in Figs. 2(d), 2(i), and 2(j), and more clearly in Fig. 1(c) for $\kappa/\omega_0 = \{0, 10^3, \infty\}$ satisfy this general condition for the period doubling instability. We emphasise that the arguments discussed so far hold only if the initial state is an eigenstate of the Hamiltonian during the bright times. Otherwise, the system will dephase and a clean period doubling dynamics will not be observed. This will be discussed further in subsection IIIC. Moreover, Eqs. (10) and (11) only apply to binary drives, in which the system becomes noninteracting at well-defined times. For smooth sinusoidal driving, we do not find any clean period doubling response for all relevant types of initial states in the absence of dissipation, as shown in Appendix D. This underscores the sensitivity to the specific driving protocol of the TC in the closed-system limit.

2. Open systems

We now discuss the results for the open Dicke model with dissipation strength $0 < \kappa/\omega_0 < 10^3$. For D = 0, the photonic and spin degrees of freedom decouple leading to a spin dynamics equivalent to the D=0 case in the LMG model. The initially nonzero photon number eventually vanishes due to dissipation. The magnetisation j_x oscillates at a frequency ω_0 around zero, as seen in Fig. 3(b), and the apparent perioddoubling for D = 0 is trivial since the periodic driving is in fact absent. We show an example of a dissipative TC in the Dicke model in Fig. 3(d), in which the specific driving parameters yield bright and dark times that are both incommensurate to the precession period, $t_{\rm bright} \approx 0.5385 T_0$ and $t_{\rm dark} \approx 0.2308T_0$, respectively. This demonstrates that the period-doubling instability conditions for the nondissipative limits based on Eqs. (10) and (11) are no longer applicable, in general, when dissipation is present.

Going from $\kappa = 0$ to $\kappa/\omega_0 = 0.1$ (Figs. 2(d) and 2(e)) we see that while time crystalline phases remain along the line defined by Eq. (10), new TCs start to emerge in other parts of the phase diagram associated with driving parameters that would otherwise lead to thermal phases in the closed DM. Moreover, some of the thermal phases for $\kappa = 0$ are converted to not only TCs but also TQCs after dissipation is introduced. Thus, we provide a concrete demonstration of dissipation, the photon decay, counteracting the heating induced by the periodic drive. Increasing the dissipation strength pushes the TCs away from the instability line in the closed-system limit as seen from the change in the phase diagram from $\kappa/\omega_0=0.1$ to $\kappa/\omega_0 = 1$, see Figs. 2(e) and 2(f). Further increase in the dissipation strength leads to an expansion of the area in phase diagram with TCs as demonstrated in Figs. 1(c) and 2(d) for $\kappa/\omega_0 \in [1, 10].$

Note, however, that the dissipation-induced enhancement of TC in the phase diagram only applies up to a certain value

of κ . In Fig. 1(c), comparing the area of the time crystalline phase in $\kappa/\omega_0=5$ and $\kappa/\omega_0=10$, we find that the TC area decreases for $\kappa/\omega_0>5$. While the overall shape of the area with both TC and TQC is not significantly changed from $\kappa/\omega_0=10$ to $\kappa/\omega_0=10^2$ as displayed in Figs. 2(g) and 2(h), there are more TQCs in the phase diagram for $\kappa/\omega_0=10^2$ than for $\kappa/\omega_0=10$, which implies that the TCs are converted to TQCs with increasing dissipation strength. This can also be inferred from the expansion of the TQC domain as the dissipation strength increases from $\kappa/\omega_0=10$ to $\kappa/\omega_0=21$ in Fig. 9(a) of Appendix B.

We have seen that for the ADM and LMG model, the TCs are restricted along the instability line Eq. (10). The question remains whether the phase diagrams for dissipative systems will change gradually or suddenly as κ increases to large enough values, such that the adiabatic approximation and thus, the ADM and LMG model can be applied. To address this issue, we consider even stronger dissipation strengths on the order of $\kappa/\omega_0 \sim 10^2$ while still solving the full semiclassical equations including the photon dynamics. For even stronger dissipation beyond the optimal value, we find that the dynamical phase diagram gradually develops features that resemble its closed-system counterpart, as seen in Figs. 1(c) and 2(d) for $\kappa/\omega_0 = 10^2$. Comparing $\kappa/\omega_0 = 10^2$ and $\kappa/\omega_0 = \{10^3, \infty\}$, some of the TQCs, which are previously TCs for weaker dissipation, turn into thermal phases in the closed-system models. Moreover, going from $\kappa/\omega_0=10$ to $\kappa/\omega_0 = 10^2$, the time crystalline phases start to gather towards the instability line Eq. (10) for closed systems.

To summarise subsection III A, we identify the condition for creating TCs in the closed-system limit with a periodic binary drive or bang-bang protocol. We also demonstrate that dissipation, in general, leads to the expansion of the TC and TQC areas in the phase diagram. The two limits $\kappa=0$ and $\kappa\to\infty$ are smoothly connected by the gradual change of the phase diagram as dissipation is increased.

B. Robustness against random driving errors

We will now investigate the role of dissipation on the robustness of TCs against temporal noise. To this end, we introduce a random driving error in the duty cycle for every Floquet drive

$$\lambda(t) = \begin{cases} \lambda_0, & nT_d \le t < (n+D_n)T_d \\ 0, & (n+D_n)T_d \le t < (n+1)T_d, \end{cases}$$
 (12)

where $D_n = D + \Delta D_n$ and ΔD_n is a random number drawn from a box distribution, $\Delta D_n \in [-\Delta D, \Delta D]$. A single realisation of this disordered drive is depicted in Fig. 4(a) (see also the inset of Fig. 4(c)). We also consider another kind of temporal perturbation, namely in the light-matter coupling strength such that

$$\lambda(t) = \begin{cases} \lambda_0 + \lambda_n, & nT_d \le t < (n+D)T_d \\ 0, & (n+D)T_d \le t < (n+1)T_d, \end{cases}$$
(13)

where $\lambda_n/\lambda_0 \in [-\Delta\lambda_0, \Delta\lambda_0]$. An example of a periodic drive with this disorder is shown in the inset of Fig. 4(e).

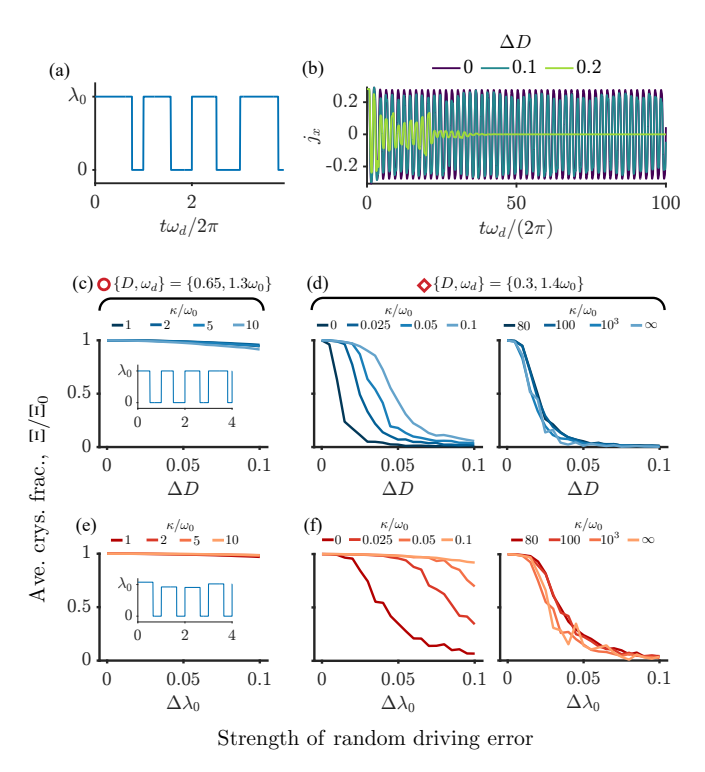


FIG. 4. (a) One realisation of the disordered drive. (b) Dynamics of the total magnetisation along the x-direction, j_x , for different disorder strengths ΔD as indicated in the legend. The driving parameters are $\{D,\omega_d\}=\{0.65,1.3\omega_0\}$ and the dissipation strength is $\kappa/\omega_0=1$. The initial state is a \mathbb{Z}_2 -symmetry broken phase for $\lambda_0=1.1\lambda_{\rm cr}$. (c),(d) Dependence of the relative crystalline fraction, Ξ/Ξ_0 , on the strength of the random driving error or temporal disorder, ΔD . (e),(f) Similar to (c) and (d) but for a noisy light-matter coupling with disorder strength $\Delta\lambda$. Insets: one realisation of the disordered drive.

In the following, we use driving parameters corresponding to the circles and diamonds in Fig. 2, where TCs exist for clean driving or in the absence of temporal disorder. We take 100 disorder realisations when calculating the dynamics of j_x and the crystalline fraction Ξ , which we define as the average of the power spectrum of j_x at $\omega_d/2$. We present in Fig. 4(b) the disorder averaged dynamics of j_x for a noisy duty cycle, Eq. (12). As the disorder strength increases, the oscillation amplitude of j_x deviates from being a constant as the TC becomes unstable. This is expressed in the reduction of the relative crystalline fraction Ξ/Ξ_0 , where Ξ_0 is the crystalline fraction in the clean case, for increasing disorder strength ΔD as shown in Figs. 4(c) and 4(d). Additional frequencies introduced by the noise broaden the power spectrum of j_x and thereby decreases the crystalline fraction. More importantly, Figs. 4(c) and 4(d) demonstrate another key finding of this work, which is the role of dissipation in making a TC more robust against temporal noise. For the nondissipative cases $\kappa/\omega_0 = \{0, 10^3, \infty\}$ in Fig. 4(d), the crystalline fraction decays rapidly with ΔD . In contrast, the decay is slower when dissipation is introduced, i.e., the crystalline fraction remains large over a wide range of disorder strengths. This is evident in Fig. 4(c) for intermediate dissipation strengths, wherein the crystalline fraction is found to slowly decrease with ΔD .

The dissipation-induced robustness against temporal noise can be understood as a consequence of the dissipation-induced expansion of the TC area in the phase diagram discussed in the previous subsection. In the phase diagram for $\kappa/\omega_0=10$ in Fig. 2(g), the TC corresponding to the driving parameters marked by the circle is surrounded by other period-doubling TCs and thus, a perturbation in D, ω_d , and ω_0 will not easily push the system into a different dynamical phase. On the other hand for closed systems, we see in Figs. 2(d), 2(i), and 2(j) that for driving parameters marked by the diamond, a slight variation in D away from the instability condition Eq. (10) will take the system to a different dynamical phase other than a perioddoubling TC. This leads to a TC that is less robust against temporal perturbations of the driving parameters D and ω_d . This also explains the relatively weak robustness observed for strong dissipation in the right panel of Fig. 4(d) since the TC area is relatively small and highly fragmented for dissipation strengths of this order of magnitude as seen for $\kappa/\omega_0=10^2$ in Fig. 1(c). In Figs. 4(e) and 4(f), we observe similar findings for a drive with noisy light-matter coupling. Both dissipative and nondissipative models appear to be more robust against this type of noise, as seen from the larger plateaus in the crystalline fractions in Fig. 4(f) compared to those in Fig. 4(d). This can be attributed to the presence of TCs even for higher values of λ_0 as seen in Fig. 10 of Appendix C.

C. Initial fully polarised states

For potential applications and experimental realisations, we discuss how close the initial state has to be to the desired state, to create a TC. So far, we have considered one of the symmetry broken states as the initial state. In Ref. [9], robustness against the choice of initial state for TCs in the kicked LMG model has been demonstrated but only for initial symmetry broken states corresponding to an interaction strength different from the one in the Hamiltonian, i.e., $\lambda(t=0) \neq \lambda_0$. Here, we explore other types of initial states, namely fully polarised states either along the positive x-direction, $\{j_x, j_y, j_z\} = \{1/2, 0, 0\}$, and negative z-direction, $\{j_x, j_y, j_z\} = \{0, 0, -1/2\}$, which we label as $|\Rightarrow\rangle$ and $|\Downarrow\rangle$, respectively. A symmetry broken state interpolates between these two limits. For the Dicke model, we include a small fluctuation in the photon mode, such that a(t=0) = 0.01.

We present in Figs. 5(a) and 5(b) the evolution of the phase diagrams as a function of the dissipation strength for initial fully polarised states $|\Rightarrow\rangle$ and $|\Downarrow\rangle$, respectively. Crucially, we find that for both types of fully polarised initial states, time crystalline phases are absent in the closed system models, $\kappa/\omega_0 = \{0, 10^3, \infty\}$, and the phase diagrams are dominated by thermal phases, see also Figs. 1(d) and 1(e). The behaviour is strikingly different for dissipative cases as seen in Fig. 5 for $\kappa/\omega_0 = \{1, 10\}$. The choice of initial state between $|\Rightarrow\rangle$ and $|\Downarrow\rangle$ does not significantly alter the area in the phase diagram with TCs. This is further emphasised if we include the initial symmetry broken state in the comparison as evidenced by the results for $\kappa/\omega_0 \in [1, 10]$ in Figs. 1(c)-1(e). This implies that

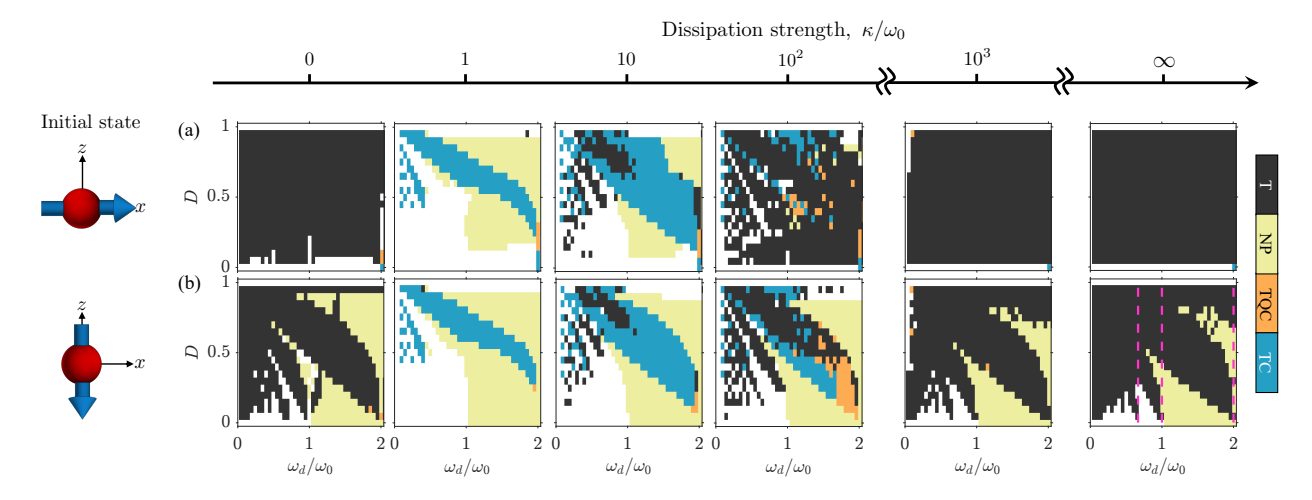


FIG. 5. Dynamical phase diagrams similar to Fig. 2 but for initial fully polarised states (a) $|\Rightarrow\rangle$ and (b) $|\Downarrow\rangle$ as schematically illustrated in the left-most panels. The dashed vertical lines in $\kappa=\infty$ denote the parametric resonance condition $\omega_d/\omega_0=2/n$, where $n=\{1,2,3\}$. The system parameters are the same as in Fig. 2.

dissipation allows for flexibility in the fidelity of the initial state preparation. In Appendix D, we observe similar results for a smooth sinusoidal or continuous driving protocol, which further corroborates the positive role of controlled dissipation for infinite-range interacting spin systems.

The results for the ADM and LMG model, κ/ω_0 $\{10^3, \infty\}$, shown in Fig. 5(b) exhibit resonance lobes reminiscent of parametric resonances that appear when the driving frequency satisfies $\omega_d/\omega_0 = 2/n$, where $n \in \mathbb{Z}^+$. Notice that in Fig. 5(b), the shape of the TC area for $\kappa/\omega_0 = 10$ is similar to that of the primary resonance lobe ($\omega_d/\omega_0=2$) for $\kappa/\omega_0 = \{10^3, \infty\}$. This points to a period-doubling instability arising from a parametric resonance as the main mechanism behind the formation of dissipative TCs with binary driving, similar to the smooth sinusoidal driving in Refs. [33, 64]. Note that the parametric resonance also applies to initial symmetry broken states as evinced by the shape of the thermal region, including the TC and TQC phases, in Fig. 2(d) for $\kappa = 0$. There, the absence of dissipation heats up the system resulting to a more prominent thermal phase except at the special points along the instability line for initial symmetry broken states, Eq. (10).

IV. QUANTUM RESULTS

We now study the TCs in the limit of small number of spins, wherein quantum effects and many-body correlations become dominant. Platforms for physical implementations of a relatively small number of artificial or effective spins include circuit QED systems based on superconducting qubits [23, 65–69] and ion chains [47–49]. In the following, we obtain the full quantum results using the QuantumOptics.jl library [70] and we employ the discrete truncated Wigner approximation (DTWA) [71, 72] for larger number of spins beyond the reach of full quantum mechanical simulations.

We focus on the initial fully polarised state along the pos-

itive x-direction $|\Rightarrow\rangle = \bigotimes_N |\to\rangle$, which in the mean-field regime corresponds to $\{j_x,j_y,j_z\}=\{1/2,0,0\}$, to gain insights on the features of TCs in the quantum regime. By comparing exact quantum and DTWA results, we will also assess the applicability of DTWA in capturing the time crystalline dynamics for periodically driven infinite-range interacting spins. For the Dicke model, the photon mode is initialised in the vacuum state $|0\rangle$, such that the initial state of the system is $|\psi(t=0)\rangle = |\Rightarrow\rangle\otimes|0\rangle$.

The results for the LMG model with N=8 spins and driving parameters $\{D,\omega_d\}=\{0.3,1.4\omega_0\}$ are depicted in Fig. 6. In Fig. 6(a) for $\lambda_0=1.1\lambda_{\rm cr}$, the system is in the thermal phase even in the mean-field limit of $N\to\infty$. This again exemplifies the importance of initialising the system in a symmetry broken eigenstate to create a TC in the closed-system limit. In the quantum regime, the irregular mean-field

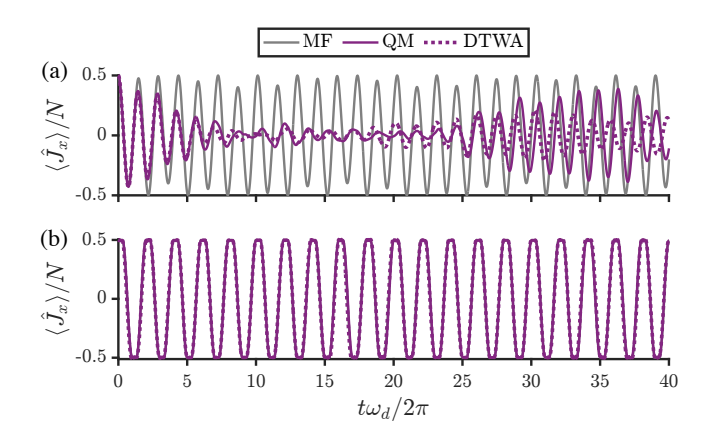


FIG. 6. Dynamics of the expectation value of the total magnetisation along the x-direction for an initial fully polarised state $|\Rightarrow\rangle$ in the LMG model. The interactions strengths are (a) $\lambda_0=1.1\lambda_{\rm cr}$ and (b) $\lambda_0=4.0\lambda_{\rm cr}$. For the exact quantum mechanical (QM) results and DTWA, the number of spins is N=8. The driving parameters are D=0.3 and $\omega_d=1.4\omega_0$.

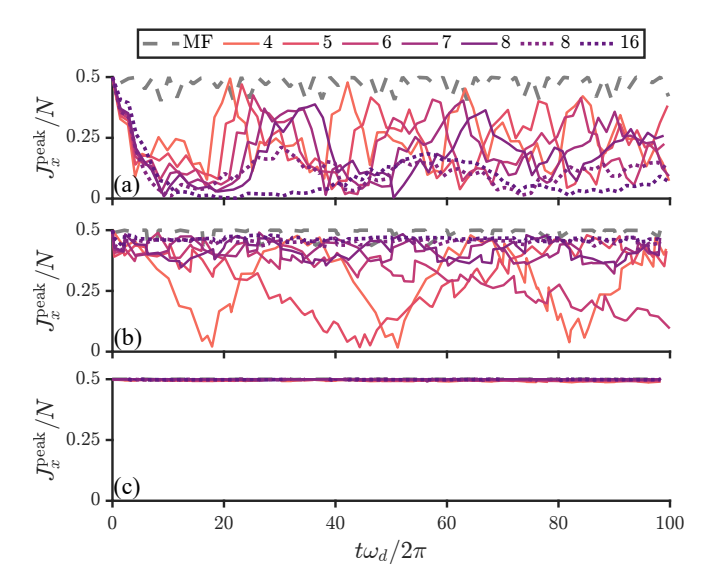


FIG. 7. Dynamics of the peaks in the total magnetisation in the LMG model for an initial state of $|\Rightarrow\rangle$. The solid (dotted) curves denote the full quantum (DTWA) results. The interactions strengths are (a) $\lambda_0=1.1\lambda_{\rm cr}$, (b) $\lambda_0=2.0\lambda_{\rm cr}$, and (c) $\lambda_0=4.0\lambda_{\rm cr}$. The driving parameters are the same as in Fig. 6.

dynamics translate into a beating of the oscillations in the expectation value of the total magnetisation $\langle \hat{J}_x \rangle/N$ similar to the behaviour found in the kicked LMG model [9]. The full quantum mechanical and DTWA results agree on the overall qualitative behaviour of the dynamics. While we find excellent agreement between the exact and DTWA results for short times, quantitative deviations appear in the long-time dynamics, which is expected in simulations of closed system quantum dynamics using phase-space methods [73].

For stronger interactions, e.g., $\lambda_0 = 4\lambda_{\rm cr}$ in Fig. 6(b), a TC is formed and interestingly, the mean-field, exact quantum, and DTWA results agree for the entire simulation time of 100 driving cycles, which is noteworthy considering the relatively small number of spins N=8. This also hints at the ability of the DTWA to capture the dynamics of TCs even for long times provided that the interactions in a fully connected model are sufficiently strong. We note that the overlap of a symmetry broken eigenstate with the fully polarised state along the xdirection increases with the interactions strength, which can also be inferred from the mean-field steady-state solution in Eq. (6). This explains the appearance of a TC in Fig. 6(b) despite the initial state not being a symmetry broken eigenstate for $\lambda_0 = 4\lambda_{\rm cr}$. Thus, we propose to utilise large interactions strengths for creating TCs in fully connected systems with few spins if, for a given platform, it is easier to prepare an initial fully polarised state.

Next, we study the dependence of the beating oscillations on the number of spins in the LMG model. To this end, we obtain the peaks in the oscillatory dynamics of the magnetisation, $J_x^{\rm peak}$, which is directly related to the envelope of the oscillations in $\langle \hat{J}_x \rangle$. In Fig. 7, we display the dynamics of $J_x^{\rm peak}$ for different N including the mean-field limit. For weak interactions, the chosen driving parameters in Fig. 7 lead to

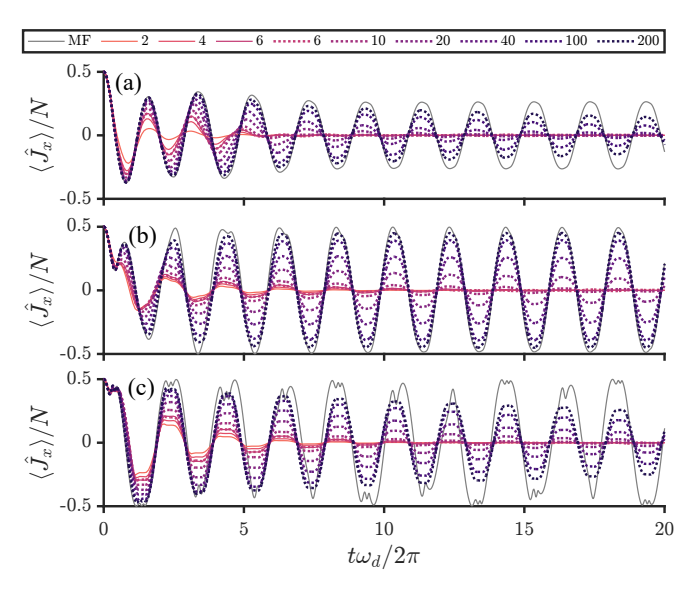


FIG. 8. Similar to Fig. 6 but for the open Dicke model with $\kappa=\omega_0$. The light-matter coupling strengths are (a) $\lambda_0=1.1\lambda_{\rm cr}$, (b) $\lambda_0=2.0\lambda_{\rm cr}$, and (c) $\lambda_0=4.0\lambda_{\rm cr}$. The photon frequency is $\omega_p=\omega_0$. The driving parameters are D=0.5 and $\omega_d=1.6\omega_0$.

irregular and therefore, non-time-crystalline dynamics. The convergence towards the mean-field limit for increasing N is slow and can only be seen at short times due to the irregularity of the long-time dynamics. The tendency towards the mean-field prediction becomes more clear for stronger interactions as seen in Fig. 7(b) for $\lambda_0=2\lambda_{\rm cr}$. In particular, we observe that the beat period increases with N implying that it becomes infinitely large as $N\to\infty$, consistent with the mean-field prediction of an infinitely-long lived TC. This behaviour is more apparent if the system is initialised in a symmetry broken eigenstate as shown in Fig. 13 of Appendix E. For sufficiently strong interactions represented by $\lambda_0=4\lambda_{\rm cr}$ in Fig. 7(b), we recover results consistent with Fig. 6(b), especially the emergence of long-lived period-doubling response for a relatively small number of spins $(N\sim4)$.

We present in Fig. 8 the quantum dynamics in the open Dicke model for $\kappa = \omega_0$. In Fig. 8(a), the driving parameters correspond to a TC in the mean-field limit. For few spins, the period-doubling oscillations rapidly decay and for N < 10, the time-translation symmetry breaking response only survives for short times, typically around five driving cycles $t \approx 5T_d$. These exponentially decaying oscillations are analogous to the beating oscillations in the closed-system limit. However, unlike the beat period in the LMG model, the decay constant characterising the exponential suppression of oscillations in the open DM does not monotonously depend on the interactions strength. This is evident from the longerlived oscillations in Fig. 8(b) compared to those in Fig. 8(c), even though λ_0 is larger in Fig. 8(c). This means that using the interactions strength to prolong the lifetime of a TC in the open Dicke model is not as efficient as in closed systems, if the driving parameters are fixed. Alternatively, increasing the number of spins could also increase the lifetime of a dissipative TC [25, 27, 74]. Indeed, we find in Fig. 8 that the decay

slows down with N, irrespective of the interactions strength. In contrast to the LMG model, in which as few as N=4 spins generate a period-doubling signal lasting for $t>10T_d$, the number of spins needed for the open Dicke model for the same timescale is N>20.

We point out that in Fig. 8(c), despite the mean-field dynamics showing irregular or chaotic behaviour, both full quantum and DTWA simulations predict periodic albeit decaying oscillations. This apparent inconsistency between mean-field and quantum approaches, regarding the presence or absence of a transition to a chaotic phase, is also reported in a driven-dissipative LMG or fully-connected Ising model [75]. Lastly, we note that for N=6 in Fig. 8, DTWA is in good agreement with the numerical data obtained from the full quantum mechanical treatment, thereby suggesting that, in dissipative scenarios, DTWA can capture time crystalline dynamics even for small N. This stabilising effect of dissipation on the performance of DTWA as a method is similar to that found in the positive-P approach for driven-dissipative bosons [76].

V. SUMMARY AND DISCUSSION

In this work, we have extensively studied the influence of dissipation on TCs in a spin system with infinite-range interactions with binary driving. In particular, we have employed both mean-field and quantum mechanical treatments of the dynamics in the open DM for different dissipation strengths. For large dissipation strengths $\kappa > 10^2$, we approximate the system as closed using the ADM and LMG model. In Table I, we summarise the key properties of TCs, specifically, robustness in the thermodynamic limit and dynamical features in the quantum limit, for the closed-system and dissipative regimes.

From our mean-field approach, we have identified a simple but finely tuned set of conditions, involving the driving parameters and initial state, for creating a period-doubling response in the closed-system limit. We have demonstrated that dissipation expands this instability line to include larger areas in parameter space. Thus, we connect the time crystal phenomenology in the open-system and the closed-system limits of the infinite-range interacting spins. Moreover, we have observed that the presence and lifetime of TCs do not monotonously depend on the dissipation strength. This implies the existence of an optimal dissipation strength for realising TCs, similar to driven-dissipative Heisenberg chains [32]. However, here we show that the optimal dissipation depends strongly on the specific choice of driving parameters and in certain cases, the absence of dissipation, $\kappa = 0$ or $\kappa \to \infty$, could in fact be the optimal choice, if one is only interested in generating a period-doubling response. If the goal, however, is to create a time crystal that is also robust against unwanted errors in the drive and imperfect preparation of the initial state, we ascertain that controlled dissipation is helpful. In particular, we find that the TC area in the phase diagram becomes relatively large for intermediate dissipation strengths $\kappa \sim \omega_0$. A large TC area in the phase diagram contributes to the robustness not only against variations in system parameters but also against noise in the drive. Furthermore, we demonstrate that

	Closed	Open
	(LMG model)	(Dicke model)
Mean-field		
Robust against:		
random errors in the drive	Weak	Strong
choice of initial state	Weak	Strong
choice of driving protocol	Weak	Strong
variation in system parameters	Strong*	Strong [†]
Quantum		
Oscillations	Beating	Exponential
		decay
Lifetime increases with	Interaction	Number of
	strength	spins

TABLE I. Summary of the properties of the period-doubling time crystals in infinite-range interacting spins. In the LMG model, "Strong*" means that it is strongly robust only for variations and random errors in the interactions strength. In the open Dicke model, "Strong†" means strong robustness only within the resonance area in the phase diagram.

dissipation can form TCs, which are insensitive to the choice of initial state. We also attribute the formation of dissipative TCs using a binary drive to a period-doubling instability of a parametric resonance and thus, we generalise the mechanism and conditions proposed in Ref. [23].

Our quantum results for finite N obtained using numerically exact calculations and the DTWA indicate an exponential decay of the period-doubling oscillations when dissipation is present. On the other hand, in the two extremes $\kappa=0$ or $\kappa\to\infty$, the TCs exhibit beating behaviour, the period of which increases with the number of spins, consistent with Ref. [9]. The scaling with the interaction strength of the lifetime of closed-system TCs is more favourable than the scaling with the number of spins for open-system TCs. This suggests a possible advantage of TCs in the closed-system limits if the underlying platform operates with few spins, albeit the driving parameters must be finely tuned according to Eq. (10).

Finally, we remark on the apparent lack of experimental evidence for TCs in the closed fully connected spin systems. As we have shown in this study, the period-doubling instability in the LMG model and the closed DM strongly depends on the specific driving protocol. For sinusoidal driving, which was utilised for the realisation of dissipative TC in the small- κ regime of a cavity-QED system [33], the DM with $\kappa=0$ and $\kappa\to\infty$ do not host any TCs as shown in Appendix D. Instead, a binary drive according to Eq. (8) is required to induce a period-doubling response but only in a narrow region in the phase diagram spanned by the driving parameters, i.e. they must follow Eq. (10). It remains to be seen whether alternative schemes that periodically drive the transverse field (as in Refs. [9, 10]), instead of the spin-spin interactions strength (as done here), would yield a larger TC area in the relevant phase

(A11)

diagram. Assuming a binary drive, high-fidelity state preparation is still required, i.e., the initial state should not veer too far from the symmetry broken state of the Hamiltonian during the bright times. For the cavity-QED system operating in the regime $\kappa\gg\omega_0$ [46], which emulates the ADM and LMG model, the above considerations for the driving protocol and initial state preparation may not be an issue. However, for this system, future studies need to address whether the large bandwidth of the cavity would cause higher momentum modes to participate in the dynamics. If so, this leads to a breakdown of the two-level approximation of the atoms and therefore, the mapping onto effective spin-1/2 particles.

ACKNOWLEDGMENTS

This work was funded by the UP System Balik PhD Program (OVPAA-BPhD-2021-04) and the Deutsche Forschungsgemeinschaft (DFG, German Research Foundation) "SFB-925" project 170620586 and the Cluster of Excellence "Advanced Imaging of Matter" (EXC 2056), Project No. 390715994. J.S. acknowledges support from the German Academic Scholarship Foundation. We thank C. Sevilla for helpful discussions.

Appendix A: Equations of motion

For a Hamiltonian \hat{H} and the type of dissipator in Eq. (2), the dynamics of the expectation value of an operator \hat{O} is

$$\partial_t \langle \hat{O} \rangle = \frac{i}{\hbar} \langle [\hat{H}, \hat{O}] \rangle + \kappa \left\langle \left(2\hat{a}^{\dagger} \hat{O} \hat{a} - \hat{a}^{\dagger} \hat{a} \hat{O} - \hat{O} \hat{a}^{\dagger} \hat{a} \right) \right\rangle. \tag{A1}$$

Within mean-field theory, we approximate $\langle \hat{a}\hat{J}_{\mu}\rangle \approx \langle \hat{a}\rangle \langle \hat{J}_{\mu}\rangle$. We present the equations of motion for the collective spins and for individual spins, as the former is used in the mean-field treatment, while the latter is used in DTWA.

1. Dicke model

The equations of motion for the Dicke model are

$$\partial_t a = -(i\omega_p + \kappa)a - i2\lambda j_x \tag{A2}$$

$$\partial_t j_x = -\omega_0 j_y \tag{A3}$$

$$\partial_t j_y = \omega_0 j_x - 2\lambda (a + a^*) j_z \tag{A4}$$

$$\partial_t j_z = 2\lambda (a + a^*) j_y \tag{A5}$$

If we decompose j_{μ} in terms of individual spins, we obtain

$$\partial_t a = -(i\omega + \kappa)a - i\lambda \frac{1}{\sqrt{N}} \sum_i s_i^x$$
 (A6)

$$\partial_t s_i^x = -\omega_0 s_i^y \tag{A7}$$

$$\partial_t s_i^y = \omega_0 s_i^x - 2\lambda \frac{1}{\sqrt{N}} (a + a^*) s_i^z \tag{A8}$$

$$\partial_t s_i^z = 2\lambda \frac{1}{\sqrt{N}} (a + a^*) s_i^y \tag{A9}$$

For beyond mean-field approaches, a fluctuation or stochastic term associated with the dissipation must be included in the equations of motion [57, 72]. In our implementation of the equations of motion governing the trajectories in the DTWA, we separate the real and imaginary components of the photon field, $a = a_{\rm R} + ia_{\rm I}$, which yields

$$da_{\rm R} = (-\kappa a_{\rm R} + \omega a_{\rm I}) dt + \sqrt{\kappa/2} dW_1 \tag{A10}$$

$$da_{\rm I} = \left(-\omega a_{\rm R} - \kappa a_{\rm I} - \frac{\lambda}{\sqrt{N}} \sum_{j} s_{j}^{x}\right) dt + \sqrt{\kappa/2} dW_{2}$$

$$\partial_t s_i^x = -\omega_0 s_i^y \tag{A12}$$

$$\partial_t s_i^y = \omega_0 s_i^x - 4\lambda \frac{1}{\sqrt{N}} a_{\rm R} s_i^z \tag{A13}$$

$$\partial_t s_i^z = 4\lambda \frac{1}{\sqrt{N}} a_{\rm R} s_i^y. \tag{A14}$$

The two independent Wiener processes W_1 and W_2 account for the stochastic noise and they satisfy $\langle dW_i \rangle = 0$ and $\langle dW_i dW_j \rangle = \delta_{i,j} dt$.

2. Atom-only Dicke model

Next, for the atom-only Dicke model in the thermodynamic limit, the equations of motion are [54, 55]

$$\partial_t j_x = -\omega_0 j_y \tag{A15}$$

$$\partial_t j_y = \omega_0 j_x + \frac{8\lambda^2 \omega}{(\kappa^2 + \omega^2)} j_x j_z + \frac{16\lambda^2 \kappa \omega_p \omega_0}{(\kappa^2 + \omega_p^2)^2} j_y j_z \quad (A16)$$

$$\partial_t j_z = -\frac{8\lambda^2 \omega}{(\kappa^2 + \omega^2)} j_x j_y - \frac{16\lambda^2 \kappa \omega_p \omega_0}{(\kappa^2 + \omega_p^2)^2} (j_y)^2$$
 (A17)

The corresponding equations for the individual spins are

$$\partial_t s_j^x = -\left[\omega_0 - \left(\frac{2\lambda^2 \omega_0(\omega_p^2 - \kappa^2)}{N(\kappa^2 + \omega_p^2)}\right)\right] s_j^y \tag{A18}$$

$$\partial_t s_j^y = \omega_0 s_j^x + \frac{4\lambda^2 \omega_p}{N(\kappa^2 + \omega_p^2)} s_j^z \sum_{i=1}^N s_i^x$$
(A19)

$$+\frac{8\lambda^2\kappa\omega_p\omega_0}{N(\kappa^2+\omega_p^2)^2}s_j^z\sum_{i=1}^Ns_i^y$$

$$\partial_t s_j^z = -\frac{4\lambda^2 \omega_p}{N(\kappa^2 + \omega_p^2)} s_j^y \sum_{i=1}^N s_i^x - \frac{8\lambda^2 \kappa \omega_p \omega_0}{N(\kappa^2 + \omega_p^2)^2} s_j^y \sum_{i=1}^N s_i^y.$$
(A20)

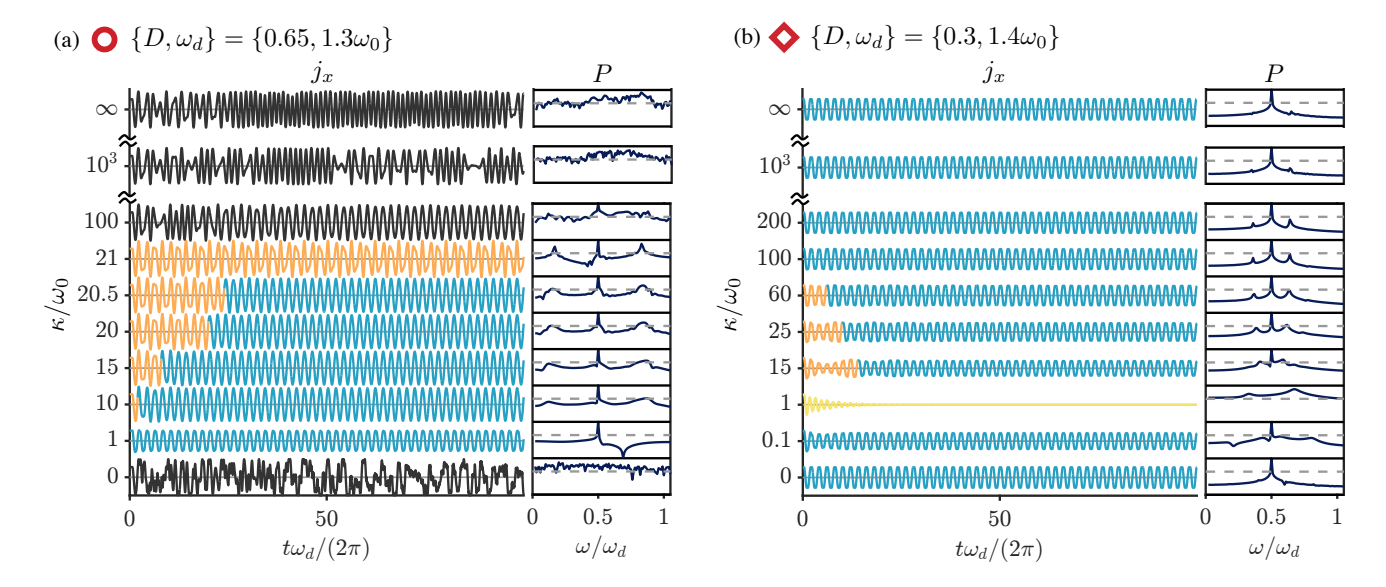


FIG. 9. Exemplary dynamics for different dissipation strengths κ with fixed driving parameters denoted by the circle and diamond in Figs. 2(d)-2(j). The left panels depict the dynamics of j_x and the right panels show the corresponding power spectrum $\log P$. The y-axis range of each plot is [-0.5, 0.5] for j_x and [-22, 0] for $\log P$. The horizontal line in the power spectrum plots denote the threshold used for identifying the presence of a TQC, which is $\log P = -8$. The remaining parameters are the same as in Fig. 2.

3. Lipkin-Meshkov-Glick model

Finally, for the LMG model, we have [51]

$$\partial_t j_x = -\omega_0 j_y \tag{A21}$$

$$\partial_t j_y = \omega_0 j_x + \frac{8\lambda^2 \omega_p}{(\kappa^2 + \omega_p^2)} j_x j_z \tag{A22}$$

$$\partial_t j_z = -\frac{8\lambda^2 \omega_p}{(\kappa^2 + \omega_p^2)} j_x j_y. \tag{A23}$$

For the individual spins, we have

$$\partial_t s_j^x = -\omega_0 s_j^y \tag{A24}$$

$$\partial_t s_j^y = \omega_0 s_j^x + \frac{4\lambda^2 \omega_p}{N(\kappa^2 + \omega_p^2)} s_j^z \sum_{i=1}^N s_i^x$$
 (A25)

$$\partial_t s_j^z = -\frac{4\lambda^2 \omega_p}{N(\kappa^2 + \omega_p^2)} s_j^y \sum_{i=1}^N s_i^x. \tag{A26}$$

Appendix B: Exemplary dynamics for different dissipation strengths

We display in Fig. 9 the exemplary dynamics for different values of dissipation strength as indicated by the labels along the vertical axis. The left panels depict the mean-field results for the time evolution of j_x for driving parameters as indicated in the figure. For the specific choice of driving parameters in Fig. 9(a), the optimal dissipation strength, identified by a response that is mostly dominated by a clean period doubling, appears to be in the intermediate range $\kappa \sim \omega_0$. As we further

increase the dissipation strength, time quasicrystalline dynamics permeate during the early times, which is signified by the appearance of extra peaks in the power spectrum. The lifetime of the TQCs increase with the dissipation rate as seen in Fig. 9 for $\kappa/\omega_0 \in [10,21]$. The system is in a thermal phase for zeroand strong-dissipation limits $\kappa/\omega_0 = \{0,10^2,10^3,\infty\}$.

In Fig. 9(b), we show the dynamics for a set of driving parameters along the instability line defined by Eq. (10). Here, we find period-doubling response in the nondissipative regimes and a light-induced normal phase for an intermediate dissipation strength $\kappa = \omega_0$.

Appendix C: Dependence on the light-matter coupling strength and photon frequency

The phase diagrams for varying dissipations strengths and coupling strengths λ are depicted in Fig. 10. We find similar results as discussed in the main text. More importantly, we demonstrate in Fig. 10 that the TCs persist for larger coupling strengths.

The results for other choices of photon frequency ω_p are shown in Fig. 11. We find that the phase diagrams for the dissipative scenarios are weakly affected by ω_p .

Appendix D: Continuous sinusoidal driving

We briefly consider a different driving protocol given by a smooth sinusoidal drive of the light-matter coupling strength,

$$\lambda(t) = \lambda_0 \left(1 + f_d \sin(\omega_d t) \right), \tag{D1}$$

where f_d is the modulation or driving strength. This protocol has been implemented to experimentally observe the

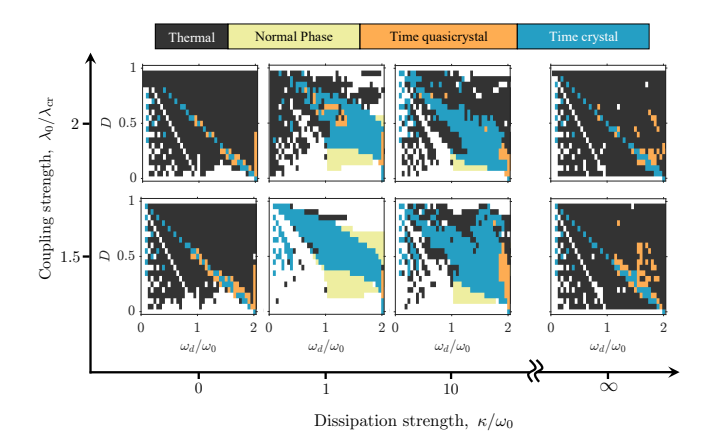


FIG. 10. Dynamical phase diagrams for different dissipation strengths. Along the vertical axis, we vary the the coupling strength and fix the frequency to $\omega_p = \omega_0$.

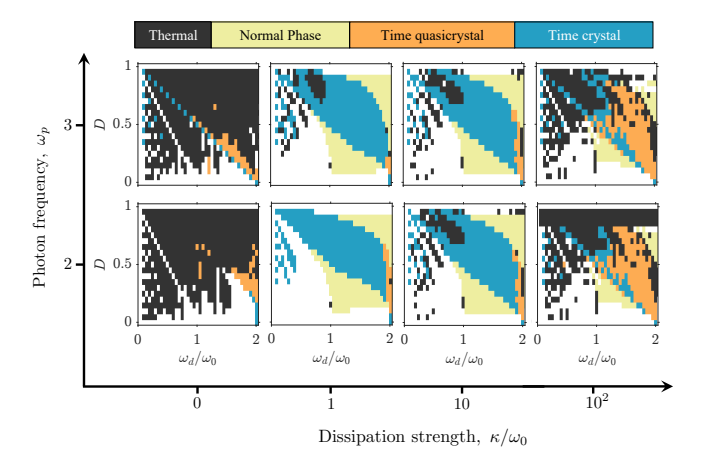


FIG. 11. Similar to Fig. 10 but for varying photon frequency along the vertical axis and fixed coupling strength $\lambda_0 = 1.1\lambda_{\rm cr}$.

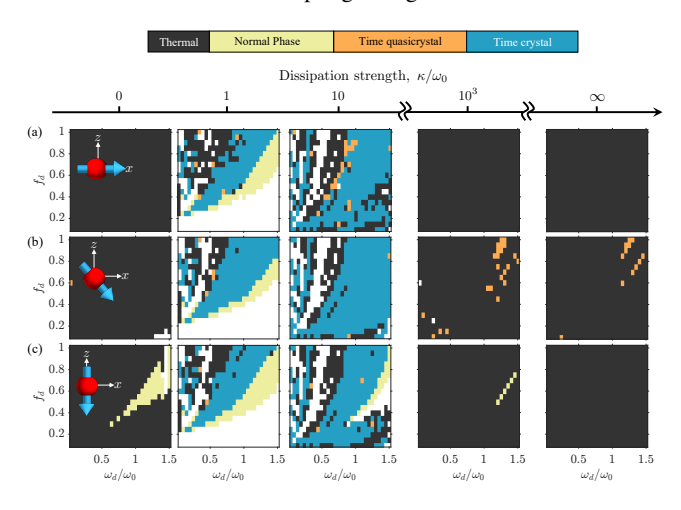


FIG. 12. Dynamical phase diagrams for a smooth sinusoidal drive and varying dissipation strengths. The remaining parameters are the same as in Fig. 2. The insets in the left-most panels depict the initial state, namely (a) fully polarised along the positive x-direction, (b) one of the symmetry broken states, and (c) fully polarised along the negative z-direction.

Dicke time crystal in the cavity-QED platform composed of Bose-Einstein condensates inside a high-finesse optical cavity pumped in the transverse direction by an optical standing wave [33].

In Fig. 12, we present the dynamical phase diagrams for such a continuous driving scheme. In addition to varying the dissipation strength, we also consider different initial states as sketched in the insets of Fig. 12. In the dissipative cases $\kappa/\omega_0=\{1,10\}$, time crystalline phases appear within the resonance lobes, which have similar shape as those found in the cavity-QED simulator for the DM [33, 50]. Contrary to the binary drive, we do not observe any TCs in the closed-system limits $\kappa/\omega_0=\{0,10^3,\infty\}$, irrespective of the initial state, for a sinusoidal drive as depicted in Fig. 12.

Appendix E: Quantum results for an initial symmetry broken state in the LMG model

The results obtained using full quantum simulations for an initial symmetry broken eigenstate are shown in Fig. 13. The driving parameters are chosen such that the system is in a time crystalline phase in the thermodynamic limit for the interactions strengths considered in Fig. 13. The beat period clearly increases with number of spins N, see Fig. 13(b). Furthermore, the dynamics shown in Fig. 7(b) appear to fluctuate around the dynamics in Fig. 13(b).

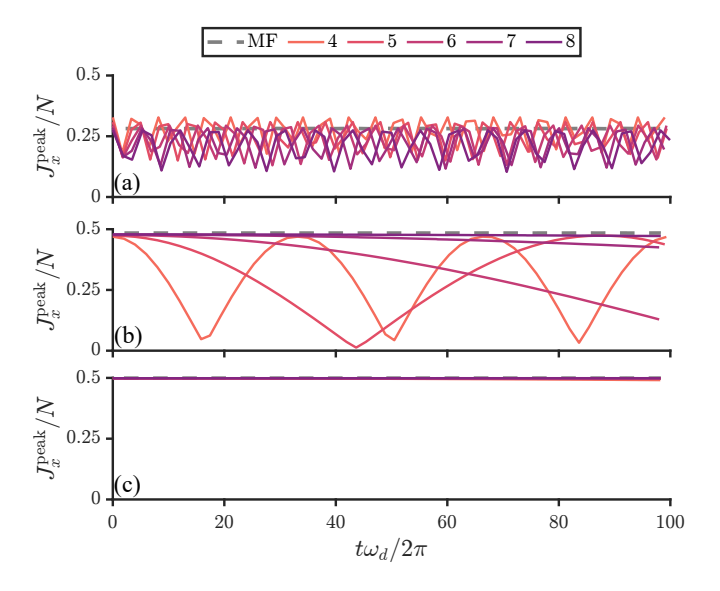


FIG. 13. Dynamics in the LMG model for an initial symmetry broken eigenstate. The interaction strengths are (a) $\lambda_0=1.1\lambda_{\rm cr}$, (b) $\lambda_0=2.0\lambda_{\rm cr}$, and (c) $\lambda_0=4.0\lambda_{\rm cr}$. The driving parameters are D=0.3 and $\omega_d=1.4\omega_0$.

- F. Wilczek, Quantum Time Crystals, Phys. Rev. Lett. 109, 160401 (2012).
- [2] K. Sacha, Modeling spontaneous breaking of time-translation symmetry, Phys. Rev. A 91, 033617 (2015).
- [3] V. Khemani, R. Moessner, and S. L. Sondhi, A Brief History of Time Crystals, arXiv e-prints, arXiv:1910.10745 (2019), arXiv:1910.10745.
- [4] D. V. Else, C. Monroe, C. Nayak, and N. Y. Yao, Discrete time crystals, Annu. Rev. Condens. Matter Phys. 11, 467 (2020).
- [5] K. Sacha, Time Crystals (Springer, Cham, 2020).
- [6] D. V. Else, B. Bauer, and C. Nayak, Floquet Time Crystals, Phys. Rev. Lett. 117, 090402 (2016).
- [7] N. Y. Yao, A. C. Potter, I.-D. Potirniche, and A. Vishwanath, Discrete Time Crystals: Rigidity, Criticality, and Realizations, Phys. Rev. Lett. 118, 030401 (2017).
- [8] V. Khemani, A. Lazarides, R. Moessner, and S. L. Sondhi, Phase Structure of Driven Quantum Systems, Phys. Rev. Lett. 116, 250401 (2016).
- [9] A. Russomanno, F. Iemini, M. Dalmonte, and R. Fazio, Floquet time crystal in the Lipkin-Meshkov-Glick model, Phys. Rev. B 95, 214307 (2017).
- [10] A. Pizzi, J. Knolle, and A. Nunnenkamp, Higher-order and fractional discrete time crystals in clean long-range interacting systems, Nat. Commun. 12, 2341 (2021).
- [11] R. E. Barfknecht, S. E. Rasmussen, A. Foerster, and N. T. Zinner, Realizing time crystals in discrete quantum few-body systems, Phys. Rev. B 99, 144304 (2019).
- [12] M. P. Estarellas, T. Osada, V. M. Bastidas, B. Renoust, K. Sanaka, W. J. Munro, and K. Nemoto, Simulating complex quantum networks with time crystals, Science Advances 6, eaay8892 (2020).
- [13] A. Pizzi, A. Nunnenkamp, and J. Knolle, Classical prethermal phases of matter, Phys. Rev. Lett. 127, 140602 (2021).
- [14] B. Ye, F. Machado, and N. Y. Yao, Floquet Phases of Matter via Classical Prethermalization, Phys. Rev. Lett. 127, 140603 (2021).
- [15] J. Zhang, P. W. Hess, A. Kyprianidis, P. Becker, A. Lee, J. Smith, G. Pagano, I.-D. Potirniche, A. C. Potter, A. Vishwanath, N. Y. Yao, and C. Monroe, Observation of a discrete time crystal, Nature 543, 217 (2017).
- [16] S. Choi, J. Choi, R. Landig, G. Kucsko, H. Zhou, J. Isoya, F. Jelezko, S. Onoda, H. Sumiya, V. Khemani, C. Von Keyserlingk, N. Y. Yao, E. Demler, and M. D. Lukin, Observation of discrete time-crystalline order in a disordered dipolar manybody system, Nature 543, 221 (2017).
- [17] J. Rovny, R. L. Blum, and S. E. Barrett, Observation of Discrete-Time-Crystal Signatures in an Ordered Dipolar Many-Body System, Phys. Rev. Lett. 120, 180603 (2018).
- [18] A. Kyprianidis, F. Machado, W. Morong, P. Becker, K. S. Collins, D. V. Else, L. Feng, P. W. Hess, C. Nayak, G. Pagano, N. Y. Yao, and C. Monroe, Observation of a prethermal discrete time crystal, Science 372, 1192 (2021).
- [19] J. Randall, C. E. Bradley, F. V. van der Gronden, A. Galicia, M. H. Abobeih, M. Markham, D. J. Twitchen, F. Machado, N. Y. Yao, and T. H. Taminiau, Many-body-localized discrete time crystal with a programmable spin-based quantum simulator, Science 374, 1474 (2021).
- [20] J. Smits, L. Liao, H. T. C. Stoof, and P. van der Straten, Observation of a Space-Time Crystal in a Superfluid Quantum Gas, Phys. Rev. Lett. 121, 185301 (2018).

- [21] S. Autti, V. B. Eltsov, and G. E. Volovik, Observation of a Time Quasicrystal and Its Transition to a Superfluid Time Crystal, Phys. Rev. Lett. 120, 215301 (2018).
- [22] B. Huang, Y.-H. Wu, and W. V. Liu, Clean Floquet Time Crystals: Models and Realizations in Cold Atoms, Phys. Rev. Lett. 120, 110603 (2018).
- [23] Z. Gong, R. Hamazaki, and M. Ueda, Discrete Time-Crystalline Order in Cavity and Circuit QED Systems, Phys. Rev. Lett. 120, 040404 (2018).
- [24] B. Zhu, J. Marino, N. Y. Yao, M. D. Lukin, and E. A. Demler, Dicke time crystals in driven-dissipative quantum many-body systems, New J. Phys. 21, 073028 (2019).
- [25] F. Iemini, A. Russomanno, J. Keeling, M. Schirò, M. Dalmonte, and R. Fazio, Boundary Time Crystals, Phys. Rev. Lett. 121, 035301 (2018).
- [26] B. Buča, J. Tindall, and D. Jaksch, Non-stationary coherent quantum many-body dynamics through dissipation, Nat. Commun. 10, 1730 (2019).
- [27] F. M. Gambetta, F. Carollo, M. Marcuzzi, J. P. Garrahan, and I. Lesanovsky, Discrete Time Crystals in the Absence of Manifest Symmetries or Disorder in Open Quantum Systems, Phys. Rev. Lett. 122, 015701 (2019).
- [28] J. O'Sullivan, O. Lunt, C. W. Zollitsch, M. L. W. Thewalt, J. J. L. Morton, and A. Pal, Signatures of discrete time crystalline order in dissipative spin ensembles, New J. Phys. 22, 085001 (2020).
- [29] J. Skulte, P. Kongkhambut, H. Keßler, A. Hemmerich, L. Mathey, and J. G. Cosme, Parametrically driven dissipative three-level Dicke model, Phys. Rev. A 104, 063705 (2021).
- [30] M. Hajdušek, P. Solanki, R. Fazio, and S. Vinjanampathy, Seeding Crystallization in Time, Phys. Rev. Lett. 128, 080603 (2022).
- [31] A. Cabot, F. Carollo, and I. Lesanovsky, Metastable discrete time-crystal resonances in a dissipative central spin system, Phys. Rev. B 106, 134311 (2022).
- [32] D. Vu and S. Das Sarma, Dissipative prethermal discrete time crystal, arXiv e-prints, arXiv:2208.01055 (2022), arXiv:2208.01055.
- [33] H. Keßler, P. Kongkhambut, C. Georges, L. Mathey, J. G. Cosme, and A. Hemmerich, Observation of a Dissipative Time Crystal, Phys. Rev. Lett. 127, 043602 (2021).
- [34] H. Keßler, J. G. Cosme, C. Georges, L. Mathey, and A. Hemmerich, From a continuous to a discrete time crystal in a dissipative atom-cavity system, New J. Phys. 22, 085002 (2020).
- [35] H. Alaeian and B. Buča, Exact multistability and dissipative time crystals in interacting fermionic lattices, Commun. Phys. 5, 318 (2022).
- [36] T. L. Heugel, M. Oscity, A. Eichler, O. Zilberberg, and R. Chitra, Classical Many-Body Time Crystals, Phys. Rev. Lett. 123, 124301 (2019).
- [37] P. Kongkhambut, J. Skulte, L. Mathey, J. G. Cosme, A. Hemmerich, and H. Keßler, Observation of a continuous time crystal, Science 377, 670 (2022).
- [38] H. Taheri, A. B. Matsko, L. Maleki, and K. Sacha, All-optical dissipative discrete time crystals, Nat. Commun. 13, 848 (2022).
- [39] H. J. Lipkin, N. Meshkov, and A. J. Glick, Validity of many-body approximation methods for a solvable model. (I). Exact solutions and perturbation theory, Nucl. Phys. 62, 188 (1965).
- [40] N. Meshkov, A. J. Glick, and H. J. Lipkin, Validity of manybody approximation methods for a solvable model. (II). Lin-

- earization procedures, Nucl. Phys. 62, 199 (1965).
- [41] A. J. Glick, H. J. Lipkin, and N. Meshkov, Validity of manybody approximation methods for a solvable model. (III). Diagram summations, Nucl. Phys. 62, 211 (1965).
- [42] R. H. Dicke, Coherence in Spontaneous Radiation Processes, Phys. Rev. 93, 99 (1954).
- [43] P. Kirton, M. M. Roses, J. Keeling, and E. G. Dalla Torre, Introduction to the Dicke Model: From Equilibrium to Nonequilibrium, and Vice Versa, Adv. Quantum Technol. 2, 1800043 (2019).
- [44] J. Larson and T. Mavrogordatos, The Jaynes-Cummings Model and Its Descendants (IOP Publishing, Bristol, 2021).
- [45] S. P. Kelly, E. Timmermans, J. Marino, and S.-W. Tsai, Stroboscopic aliasing in long-range interacting quantum systems, SciPost Phys. Core 4, 021 (2021).
- [46] K. Baumann, C. Guerlin, F. Brennecke, and T. Esslinger, Dicke quantum phase transition with a superfluid gas in an optical cavity, Nature 464, 1301 (2010).
- [47] S. Korenblit, D. Kafri, W. C. Campbell, R. Islam, E. E. Edwards, Z. X. Gong, G. D. Lin, L. M. Duan, J. Kim, K. Kim, and C. Monroe, Quantum simulation of spin models on an arbitrary lattice with trapped ions, New J. Phys. 14, 095024 (2012).
- [48] P. Jurcevic, H. Shen, P. Hauke, C. Maier, T. Brydges, C. Hempel, B. P. Lanyon, M. Heyl, R. Blatt, and C. F. Roos, Direct observation of dynamical quantum phase transitions in an interacting many-body system, Phys. Rev. Lett. 119, 080501 (2017).
- [49] C. Monroe, W. C. Campbell, L.-M. Duan, Z.-X. Gong, A. V. Gorshkov, P. W. Hess, R. Islam, K. Kim, N. M. Linke, G. Pagano, P. Richerme, C. Senko, and N. Y. Yao, Programmable quantum simulations of spin systems with trapped ions, Rev. Mod. Phys. 93, 025001 (2021).
- [50] R. J. L. Tuquero, J. Skulte, L. Mathey, and J. G. Cosme, Dissipative time crystal in an atom-cavity system: Influence of trap and competing interactions, Phys. Rev. A 105, 043311 (2022).
- [51] S. Morrison and A. S. Parkins, Dynamical Quantum Phase Transitions in the Dissipative Lipkin-Meshkov-Glick Model with Proposed Realization in Optical Cavity QED, Phys. Rev. Lett. 100, 040403 (2008).
- [52] J. Keeling, M. J. Bhaseen, and B. D. Simons, Collective Dynamics of Bose-Einstein Condensates in Optical Cavities, Phys. Rev. Lett. 105, 043001 (2010).
- [53] F. Dimer, B. Estienne, A. S. Parkins, and H. J. Carmichael, Proposed realization of the Dicke-model quantum phase transition in an optical cavity QED system, Phys. Rev. A 75, 013804 (2007).
- [54] F. Damanet, A. J. Daley, and J. Keeling, Atom-only descriptions of the driven-dissipative Dicke model, Phys. Rev. A 99, 033845 (2019).
- [55] S. B. Jäger, T. Schmit, G. Morigi, M. J. Holland, and R. Betzholz, Lindblad Master Equations for Quantum Systems Coupled to Dissipative Bosonic Modes, Phys. Rev. Lett. 129, 063601 (2022).
- [56] G. Engelhardt, V. M. Bastidas, C. Emary, and T. Brandes, acdriven quantum phase transition in the lipkin-meshkov-glick model, Phys. Rev. E 87, 052110 (2013).
- [57] H. Ritsch, P. Domokos, F. Brennecke, and T. Esslinger, Cold atoms in cavity-generated dynamical optical potentials, Rev. Mod. Phys. 85, 553 (2013).
- [58] F. Mivehvar, F. Piazza, T. Donner, and H. Ritsch, Cavity QED with quantum gases: new paradigms in many-body physics, Adv. Phys. 70, 1 (2021).

- [59] J. Klinder, H. Keßler, M. Wolke, L. Mathey, and A. Hemmerich, Dynamical phase transition in the open Dicke model, Proc. Natl. Acad. Sci. USA 112, 3290 (2015).
- [60] L. D'Alessio and M. Rigol, Long-time Behavior of Isolated Periodically Driven Interacting Lattice Systems, Phys. Rev. X 4, 041048 (2014).
- [61] M. Bukov, L. D'Alessio, and A. Polkovnikov, Universal high-frequency behavior of periodically driven systems: from dynamical stabilization to Floquet engineering, Adv. Phys. 64, 139 (2015).
- [62] A. Pizzi, J. Knolle, and A. Nunnenkamp, Period-n discrete time crystals and quasicrystals with ultracold bosons, Phys. Rev. Lett. 123, 150601 (2019).
- [63] A. Pizzi, A. Nunnenkamp, and J. Knolle, Classical approaches to prethermal discrete time crystals in one, two, and three dimensions, Phys. Rev. B 104, 094308 (2021).
- [64] R. Chitra and O. Zilberberg, Dynamical many-body phases of the parametrically driven, dissipative Dicke model, Phys. Rev. A 92, 023815 (2015).
- [65] A. Blais, J. Gambetta, A. Wallraff, D. I. Schuster, S. M. Girvin, M. H. Devoret, and R. J. Schoelkopf, Quantum-information processing with circuit quantum electrodynamics, Phys. Rev. A 75, 032329 (2007).
- [66] J. A. Mlynek, A. A. Abdumalikov, C. Eichler, and A. Wallraff, Observation of Dicke superradiance for two artificial atoms in a cavity with high decay rate, Nat. Commun. 5, 5186 (2014).
- [67] M. Bamba, K. Inomata, and Y. Nakamura, Superradiant phase transition in a superconducting circuit in thermal equilibrium, Phys. Rev. Lett. 117, 173601 (2016).
- [68] P. Forn-Díaz, J. J. García-Ripoll, B. Peropadre, J. L. Orgiazzi, M. A. Yurtalan, R. Belyansky, C. M. Wilson, and A. Lupascu, Ultrastrong coupling of a single artificial atom to an electromagnetic continuum in the nonperturbative regime, Nat. Phys. 13, 39 (2017).
- [69] F. Yoshihara, T. Fuse, S. Ashhab, K. Kakuyanagi, S. Saito, and K. Semba, Superconducting qubit-oscillator circuit beyond the ultrastrong-coupling regime, Nat. Phys. 13, 44 (2017).
- [70] S. Krämer, D. Plankensteiner, L. Ostermann, and H. Ritsch, QuantumOptics. jl: A Julia framework for simulating open quantum systems, Computer Physics Communications 227, 109 (2018).
- [71] J. Schachenmayer, A. Pikovski, and A. M. Rey, Many-Body Quantum Spin Dynamics with Monte Carlo Trajectories on a Discrete Phase Space, Phys. Rev. X 5, 011022 (2015).
- [72] J. Huber, A. M. Rey, and P. Rabl, Realistic simulations of spin squeezing and cooperative coupling effects in large ensembles of interacting two-level systems, Phys. Rev. A 105, 013716 (2022).
- [73] A. Polkovnikov, Phase space representation of quantum dynamics, Ann. Phys. 325, 1790 (2010).
- [74] K. Tucker, B. Zhu, R. J. Lewis-Swan, J. Marino, F. Jimenez, J. G. Restrepo, and A. M. Rey, Shattered time: can a dissipative time crystal survive many-body correlations?, New J. Phys. 20, 123003 (2018).
- [75] N. Zhihao, Q. Wu, Q. Wang, G. Xianlong, and P. Wang, The failure of semiclassical approach in the dissipative fullyconnected Ising model, arXiv e-prints, arXiv:2302.04381 (2023), 2302.04381.
- [76] P. Deuar, A. Ferrier, M. Matuszewski, G. Orso, and M. H. Szymańska, Fully quantum scalable description of driven-dissipative lattice models, PRX Quantum 2, 010319 (2021).